Viscous exchange flows

Gary P. Matson and Andrew J. Hogg

Citation: Phys. Fluids **24**, 023102 (2012); doi: 10.1063/1.3685723
View online: http://dx.doi.org/10.1063/1.3685723
View Table of Contents: http://pof.aip.org/resource/1/PHFLE6/v24/i2
Published by the American Institute of Physics.

Viscous exchange flows

Gary P. Matson and Andrew J. Hogg
Centre for Environmental and Geophysical Flows, School of Mathematics, University of Bristol, University Walk, Bristol BS8 1TW, United Kingdom

(Received 14 April 2011; accepted 7 September 2011; published online 24 February 2012)

Gravitationally driven exchange flows of viscous fluids with different densities are analysed theoretically and investigated experimentally within a horizontal channel. Following initiation from rest when there is a vertical boundary dividing the two fluids, the denser fluid slumps under the less dense along the underlying boundary, while the less dense fluid intrudes along the upper boundary. The motion is driven by the pressure gradients associated with the density differences between the two fluids, resisted by viscous stresses, and mathematically modelled by a similarity solution that depends on the ratio of the viscosities of the two fluids. When the viscosity of the less dense fluid is much smaller than the viscosity of the denser fluid, the shape of the interface between the fluids varies rapidly close to the upper boundary and depends weakly on the viscosity ratio within the interior of the flow. Matched asymptotic expansions are employed in this regime to determine the shape of the interface and the rates of its propagation along the boundaries. The similarity solutions are shown to be linearly stable and thus are expected to represent the intermediate asymptotics of the flow. Experiments confirm the similarity form of solutions and demonstrate close agreement with the theoretical predictions when the viscosities of the fluids are comparable, but exhibit some discrepancies when the viscosities differ more substantially. It is suggested that these discrepancies may be due to mixing between the fluids close to the boundaries, which is induced by the no-slip boundary condition. Exchange flows within porous domains are also investigated to determine the shape of the interface as a function of the ratio of the viscosities of the two fluids and using asymptotic analysis, this shape is determined when this ratio is much larger, or smaller, than unity. [http://dx.doi.org/10.1063/1.3685723]

I. INTRODUCTION

Gravitationally driven exchange flows, in which fluids of differing densities, and possibly viscosities, counter-flow within a horizontal channel, are found in many industrial and environmental settings and in this study we focus on viscously dominated motion. Applications include the various miscible displacement processes that occur in oil wells,[1] as well as geological settings, in which lavas of different consistencies interact.[2] The dynamics of viscously controlled exchanges of fluid are also relevant to flow in engineered devices of small physical size. Although the dynamics of many microfluidic devices are controlled by surface forces and diffusion processes,[3] there are nevertheless systems designed to analyse microchemical and microbiological substances, in which liquids of different densities and viscosities encounter one another and their motion is strongly affected by gravitational and viscous forces.[4]

Studies of co-flowing fluids that differ in density and viscosity abound. For example, motivated by the recovery of oil from porous subsurface reservoirs, Saffman and Taylor[5] studied the displacement of one fluid by another and established that the interface between the fluids was unstable if the viscosity of the displacing fluid was less than that of the fluid being displaced. Pumping of multi-component viscous oils along pipelines has received considerable attention (e.g., Ref. 6) with particular focus on fully developed flows of two fluids along pipes of circular cross sections (see

Ng *et al.*[7] and references therein). Studies of steady co-flowing fluids have constructed the laminar velocity fields using numerical and analytical techniques.[7–10] It has been shown that fully developed, unidirectional, axial co-flows of fluids with different material properties are often unstable[6,11,12] and recent laboratory experiments have revealed the complex ways in which the instabilities can develop.[13]

Steady counter flowing fluids within a channel can also occur, if, for example, the channel is vertically aligned and the fluids differ in density (see Refs. 14–16). These fluid motions differ from their co-flowing counterparts because they are not driven by an imposed external pressure gradient and lead to a steady exchange, but the theoretical form of the interface between them is not fully determined by the equations governing the conservation of mass and momentum. Interestingly, Kerswell[16] investigated these bidirectional flow fields in a pipe of circular cross section using quasi-analytical means and identified the shape of interface that maximised rate of exchange of the fluids. These predictions were borne out by some, but not all, of the experimental observations.[14,16]

In this paper we analyse the gravitationally driven, exchange flow within horizontal channels between fluids of differing viscosities. The density contrast leads to the denser fluid residing as a connected region adjacent to the basal boundary and slumping unsteadily under the less dense, which then flows in the opposite direction to conserve mass. Molecular diffusion between the fluids is assumed to be sufficiently weak so that the interface between them remains sharp – and the calculation of the unsteady shape of this interface is the aim of the mathematical models of this motion. Aspects of this motion have been explored recently both experimentally and theoretically.[1,17,18] Seon *et al.*[17] studied exchange flows in pipes of circular cross section and showed that when the pipe is horizontal the length of the intruding dense fluid initially grew linearly with the time from release, t, as the fluid inertia balanced the gravitational forces, before slowing and spreading as $t^{1/2}$ when the viscous and gravitational processes processes were dominant. They presented a quasi-analytical similarity solution for the latter phase of the motion, by employing an approximate solution for the axial flow of a partially filled pipe. Taghavi *et al.*[1] analysed the motion in a two-dimensional channel and showed how the ratio of the viscosities of the two fluids affected the evolution of the shape of the interface between them. Both Seon *et al.*[17] and Taghavi *et al.*[1] also investigated what type of spreading might occur if the tube were tilted or if an external flow were imposed. Finally, the recent contribution of Martin *et al.*[18] has examined an exchange flow between fluids of identical viscosity within a horizontal channel of rectangular cross section. They established theoretical predictions for the time evolution of the interface between the fluids and confirmed these predictions through laboratory experimentation. We note that the progressive evolution of a horizontal exchange flow from a dynamical state in which the fluid inertia balances buoyancy forces to one in which viscous stresses balance buoyancy forces shares some features with the free-surface spreading of viscous gravity currents,[19,20] but in the scenario of primary interest here, the motion of both fluids and the confining upper boundary influence the motion.

This study adds to the recent contributions on unsteady viscous exchange flows in horizontal channels in three ways. First, we analyse flows within three-dimensional channels and pipes; for channels of rectangular cross sections, following,[18] we demonstrate the effects of lateral side walls and for pipes of circular cross-section we extend the analysis of Seon *et al.*[17] to employ exact representations of the flow fields. Importantly, however, our analysis includes the possibility of a contrast in the viscosity of the two fluids, which was not included by Seon *et al.*[17] or Martin *et al.*[18] Our methodology can be readily applied to channels of any cross section. Second, we construct similarity solutions for the time dependent shape of the interface and asymptotically investigate the spreading when the viscosity of the less dense fluid is vanishingly small. This regime establishes the important analytical connection with the results for slumps of liquid along a horizontal boundary under an ambient gas, which have been previously modelled on the assumption that the gas is inviscid.[20,21] The asymptotic analysis admits analytical expressions for the rates of spreading that may be applied for quite a wide range of ratios of the viscosity between the two fluids. Finally, we present the results of laboratory experiments that investigate the exchange flow within rectangular channels when the fluids differ in both density and viscosity.

We note that our analysis may be related directly to gravitationally driven exchange flows in porous media, bounded above and below by impermeable surfaces. Examples of this problem in-

clude the displacement and pollution of freshwater bodies by dense saline water[22] and the injection of liquid carbon dioxide into deep aquifers to re-mediate atmospheric emissions of CO_2.[23,24] Such motions have been modelled by Huppert and Woods[25] for fluids of equal viscosities and by Hesse *et al.*[23] when the viscosities differ. Mathematically we may recover the model of flow through porous media governed by Darcy's law by examining flows within narrow channels, when the width of its cross section is much less than their height – and this simplification leads to governing equations identical to those studied by Hesse *et al.*[23] This regime was considered by Martin *et al.*[18] who demonstrated that the Brinkman extension to Darcy's law may be important for the interpretation of laboratory data in this configuration. Using the methods of this paper we examine the form of the interface between the fluids in the regime, for which the viscosities are of very different magnitudes and thus deduce asymptotic results that improve upon the empirical relations developed by Hesse *et al.*[23]

The paper is structured as follows. First, we formulate the mathematical model for the unsteady motion, based on the shallowness of the flowing layer (Sec. II). This approach yields a governing equation for the shape of the interface between the two fluids, for which similarity solutions may be constructed for flows in channels of rectangular and circular cross sections (Sec. III). A key parameter in the determination of these solutions is the ratio of the viscosities of the fluids and the shape of the interface is calculated numerically for a range of viscosity ratios. This numerical computation is simplified by interchanging the dependent and independent variables, a transformation that also permits the asymptotic determination of the shape of the interface when the viscosity of one of the fluids far exceeds the other. Comparison is made between the theoretical predictions and laboratory measurements of these flows (Sec. IV). We also include the Appendix in which viscously dominated exchange flows are analysed when the upper boundary is a free surface. The replacement of a no-slip condition at this boundary with a condition of vanishing shear stress introduces some changes to the model, although these flows are amenable to the same type of analysis as in the rest of this paper.

II. FORMULATION

The two fluids reside in an infinitely long, horizontal channel that has rigid, impermeable boundaries (see Figure 1). We orientate the (x, y, z)-coordinate system such that the x-axis is horizontal and aligned with the axis of the channel, the y-axis is horizontal and perpendicular to the axis of the channel, and the z-axis is vertical, with the lowermost point of the boundary at $z = 0$ and the uppermost at $z = d$. The interface between the two fluids is at $z = h(x, t)$. Potentially this interface could also depend upon the lateral coordinate, y, but when the flow is purely axial and the diffusion of chemical or other species that causes the density difference, and surface tension are negligible, there are no possible dynamical balances to such a lateral pressure gradient and so to leading order the interface is independent of the lateral coordinate.

Initially ($t = 0$) there is a vertical boundary at $x = 0$ between the two fluids, with the fluid of density ρ and viscosity μ_1 occupying the region $x < 0$, and the fluid of density $\rho - \Delta\rho$ (with $\Delta\rho > 0$) and viscosity μ_2 occupying $x > 0$. The system then evolves ($t > 0$) and due to buoyancy forces associated with their density difference, the denser fluid slumps into the region $x > 0$ with velocity u_1, displacing the less dense fluid which propagates above the denser fluid into $x < 0$,

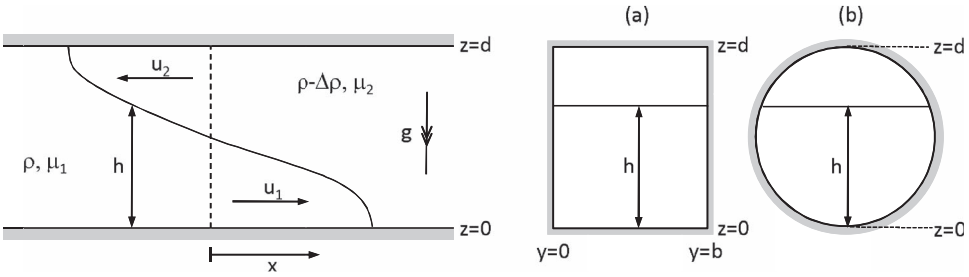

FIG. 1. The configuration of the density-driven exchange flows in (a) channels of rectangular cross section and (b) pipes with circular cross sections.

with velocity u_2. Throughout this propagation, we assume that the interface between the two fluids remains sharp, thus requiring that the diffusivity (κ) of chemical species, or other agents causing the density difference, is negligible. This effect is measured in dimensionless terms by the requirement for the Peclet number $ud/\kappa \gg 1$, where u is a velocity scale of the ensuing motion.

The model of this gravitationally driven exchange flow is based upon the lubrication approximation, whereby the streamwise lengthscale of the motion far exceeds the vertical and lateral lengthscales. This assumption implies that the flow is predominantly parallel with the channel axis and that the pressure, $p(x, z, t)$, adopts a hydrostatic distribution, attaining an as yet undetermined pressure $p_t(x, t)$ on the upper boundary $z = d$. Demanding the pressure field is continuous across the interface between the two fluids, because surface tension is assumed negligible, we find that

$$p(x, z, t) = \begin{cases} p_t(x, t) + (\rho - \Delta\rho)g(d - h) + \rho g(h - z), & 0 < z \leq h(x, t), \\ p_t(x, t) + (\rho - \Delta\rho)g(d - z), & h(x, t) < z < d. \end{cases} \tag{2.1}$$

The streamwise pressure gradient is balanced by the divergence of viscous stresses; fluid inertia is assumed to be negligible. This neglect of inertia and assumption of hydrostatic balance may be invalid during the initial phases of the motion, but we demonstrate below that they are appropriate assumptions for the long time evolution of the interface. The leading-order terms of the horizontal components of the momentum equations are given by

$$\mu_1 \nabla_\perp^2 u_1 = \frac{\partial p_t}{\partial x} + \Delta\rho g \frac{\partial h}{\partial x}, \qquad 0 < z < h(x, t), \tag{2.2a}$$

$$\mu_2 \nabla_\perp^2 u_2 = \frac{\partial p_t}{\partial x}, \qquad h(x, t) < z < d, \tag{2.2b}$$

where $\nabla_\perp^2 \equiv \partial^2/\partial y^2 + \partial^2/\partial z^2$. The equations are integrated subject to the interfacial conditions that the velocity and shear stress are continuous and to the no-slip condition on the boundaries of the channel. The volume flux of fluid carried by each layer, $q_i(x, t)$, is given by

$$q_1 = \int_{S_1} u_1 \, \mathrm{d}S \qquad \text{and} \qquad q_2 = \int_{S_2} u_2 \, \mathrm{d}S, \tag{2.3}$$

where S_1 is the cross-sectional area within the channel below the interface ($0 < z < h$) and S_2 is the cross-sectional area within the channel above the interface ($h < z < d$). Conservation of fluid mass within layer then implies that

$$\frac{\partial a}{\partial t} + \frac{\partial q_1}{\partial x} = 0 \qquad \text{and} \qquad \frac{\partial (a_t - a)}{\partial t} + \frac{\partial q_2}{\partial x} = 0, \tag{2.4}$$

where $a = \int_{S_1} \mathrm{d}S$ and $a_t = \int_{S_1 \cup S_2} \mathrm{d}S$. Summing these two evolution equations yields the condition of vanishing total volume flux in the channel ($q_1 + q_2 = 0$).

At this stage it is convenient to introduce dimensionless variables: we use d and $\mu_1/[\Delta\rho g d]$ as the length and time scale, respectively, and define the dimensionless variables

$$(X, Y, Z) = (x/d, y/d, z/d), \quad T = (\Delta\rho g d/\mu_1)t, \quad H = h/d, \quad A = a/d^2, \quad A_t = a_t/d^2,$$
$$Q_i = (\Delta\rho g d^4/\mu_1)^{-1} q_i, \quad P_t = (\Delta\rho g d)^{-1} p_t, \quad \text{and} \quad r = \mu_2/\mu_1. \tag{2.5}$$

The governing equations (2.2a) and (2.2b) are linear and thus the dimensionless volume flux of fluid in the lower layer, Q_1, is linearly proportional to the gradient of the interface,

$$Q_1 = -F(H; r)\frac{\partial H}{\partial X}. \tag{2.6}$$

The flux function F may also depend upon geometrical parameters that characterise the channel through which the fluid flows. For example, if the channel is rectangular in cross section then F will also depend upon the dimensionless width $B = b/d$. There are symmetries in this flux function given by

$$F(1 - H, r) = \frac{1}{r} F\left(H, \frac{1}{r}\right), \tag{2.7}$$

which can be readily established from the governing equations (2.2). This feature implies that in the results that follow we need only consider the solution for $r \leq 1$. Given Eqs. (2.4) and (2.6), the dimensionless nonlinear diffusion equation governing the evolution of the interface is

$$\frac{\partial A}{\partial T} = \frac{\partial}{\partial X}\left(F\frac{\partial H}{\partial X}\right), \tag{2.8}$$

which relates the change in area available for the invading dense fluid to divergence of the flux. The flux function, F, vanishes when the interface intersects the lower and upper boundaries, which occurs at $X = X_b(T)$ and $X = X_t(T)$, respectively; both of these positions emerge as part of the solution to Eq. (2.8). The equation set is closed by relating A to H, which enters through geometric considerations as indicated below (Sec. III).

It is convenient to re-formulate Eq. (2.8) by writing $X \equiv X(A, T)$, which is possible because the interface varies monotonically with distance (see Sec. III). Then, defining

$$\Psi(A, T) = \int_0^A X(A', T)\, \mathrm{d}A', \tag{2.9}$$

we find that the flow is governed by

$$\frac{\partial \Psi}{\partial T}\frac{\partial^2 \Psi}{\partial A^2} = -F\frac{\partial H}{\partial A} = -\hat{F}(A), \tag{2.10}$$

subject to the boundary conditions $\Psi(0, T) = \Psi(A_t, T) = 0$ (the latter expresses global conservation of volume), together with the initial condition $\Psi(H, 0) = 0$.

The governing equation admits similarity solutions of the form $\Psi(A, T) = T^{1/2}\Phi(A)$ and thus $X^2 \sim T$; we construct the form of the similarity solutions below for channels of rectangular (Sec. III A) and circular (Sec. III B) cross sections. It is also convenient to introduce the similarity variable $\eta = X/T^{1/2}$, noting that $\eta_t = X_t/T^{1/2}$ and $\eta_b = X_b/T^{1/2}$ represent the positions at which the interface between the fluids meets the upper and lower boundaries, respectively. In terms of these dimensionless variables, η_t and η_b depend only on the viscosity ratio, r, and possibly additional parameters that characterise the geometry of the channel, such as the dimensionless channel width B. The similarity function, $\Phi(A)$, satisfies

$$\Phi\Phi'' = -2\hat{F}, \quad \text{subject to} \quad \Phi(0) = \Phi(A_t) = 0, \tag{2.11}$$

where a prime now denotes differentiation with respect to A. This boundary value problem may be readily integrated numerically, noting that some care is required at the boundary points where Φ vanishes. We tackle this numerically by setting $\Phi(0) = \Phi(A_t) = \delta$, where δ is a non-zero, positive constant and we progressively reduce δ until a converged solution is found, which in this case is determined by demanding that $\Phi'(0)$ has become independent of δ to within a prescribed tolerance.

Before presenting these similarity solutions, we first assess the dynamical regimes and time scales over which we anticipate the similarity solution to be an accurate representation of the flow. Returning to dimensional variables, these flows are driven by the streamwise pressure gradient associated with the density difference ($\Delta\rho g\partial h/\partial x \approx \Delta\rho g d/x$), which may be balanced by the divergence of viscous stresses ($\mu\partial^2 u/\partial z^2 \approx \mu u/d^2$) or by the inertia ($\rho u\partial u/\partial x \approx \rho u^2/x$). Balancing the pressure gradient and the divergence of the viscous stresses yields the scaling relationship that underlies the similarity solution identified above and is constructed in Sec. III, namely,

$$x^2 \sim \frac{\Delta\rho g d^3}{\mu}t. \tag{2.12}$$

Under this relationship the ratio of the viscous to inertial terms, $\mu t/[\rho d^2]$, is much larger than unity and thus the balance (2.12) is valid provided

$$t \gg t_i \equiv \frac{\rho d^2}{\mu}. \tag{2.13}$$

The dynamical model is also based upon the assumption that the pressure is hydrostatic to leading order. This assumption requires that $x \gg d$, which is valid when

$$t \gg t_h \equiv \frac{\mu}{\Delta\rho g d}. \tag{2.14}$$

Using typical parameter values of the system that will be explored experimentally (Sec. IV), we have $\rho \approx 10^3\,\mathrm{kg\,m^{-3}}$, $\Delta\rho \approx 10\,\mathrm{kg\,m^{-3}}$, $g \approx 10\,\mathrm{m\,s^{-2}}$, $\mu \approx 10\,\mathrm{Pa\,s}$, and $d \approx 10^{-1}\,\mathrm{m}$ and thus the inertial time scale $t_i = 1\,\mathrm{s}$ and the time scale for non-hydrostatic effects, $t_h = 1\,\mathrm{s}$. Thus, we anticipate that on time scales longer than 1 s, the motion will be governed by a balance between the density-induced pressure gradient and the divergence of the viscous stresses and will exhibit the similarity solution derived below.

It is also straightforward to demonstrate the linear stability of the similarity solution. Following,[26,27] we introduce $\Psi = \sqrt{T}[\Phi(A) + \hat{\delta}\psi_1(A, T)]$, where the ordering parameter is assumed small ($\hat{\delta} \ll 1$). Then at $O(\hat{\delta})$, we find

$$\Phi\frac{\partial^2\psi_1}{\partial A^2} + \left(\psi_1 + 2T\frac{\partial\psi_1}{\partial T}\right)\frac{\mathrm{d}^2\Phi}{\mathrm{d}A^2} = 0\,, \tag{2.15}$$

with the boundary conditions $\psi_1(0, T) = \psi_1(A_t, T) = 0$. Since Eq. (2.15) is linear we find that $\psi_1(A, T) = T^\lambda\tilde{\psi}_1(A)$ for an as yet undetermined eigenvalue λ and $\tilde{\psi}_1(A)$ satisfies the ordinary differential equation

$$\frac{\mathrm{d}^2\tilde{\psi}_1}{\mathrm{d}A^2} = -\frac{(1+2\lambda)}{\Phi}\frac{\mathrm{d}^2\Phi}{\mathrm{d}A^2}\tilde{\psi}_1\,. \tag{2.16}$$

We demonstrate stability by forming the following integrated form of the equation:

$$-\int_0^{A_t}\frac{\mathrm{d}\tilde{\psi}_1^*}{\mathrm{d}A}\frac{\mathrm{d}\tilde{\psi}_1}{\mathrm{d}A}\,\mathrm{d}A = 2(1+2\lambda)\int_0^{A_t}\frac{\hat{F}\tilde{\psi}_1^*\tilde{\psi}_1}{\Phi}\,\mathrm{d}A, \tag{2.17}$$

where * denotes complex conjugation. Since all of the integrands are positive for $0 \le A \le A_t$, this implies that $1 + 2\lambda \le 0$ and hence the similarity solution is linearly stable. This provides the theoretical basis for the numerical evidence presented by Hesse *et al.*,[23] which demonstrated that the similarity solution is attained from initial conditions for exchange flows within porous domains. For each of the flow configurations analysed below, it is possible to evaluate numerically the eigenvalues and eigenfunctions. We comment that for each of the cases analysed with $r < 1$, we found that $|\frac{\partial\tilde{\psi}_1}{\partial H}(1)| > |\frac{\partial\tilde{\psi}_1}{\partial H}(0)|$. This implies that the perturbation to the position at which the interface intersects the upper boundary is larger than the perturbation to the position at which the interface intersects the lower boundary.

III. SIMILARITY SOLUTIONS

A. Channels with rectangular cross sections

In this section we analyse motion in channels of rectangular cross sections of dimensionless width B. The cross-sectional area $A = BH$ and so with such simple geometry it is convenient to write $\Psi = BT^{1/2}\Phi(H)$ and treat the similarity solution as a function of the interface height. The similarity solution, $\Phi(H)$, is determined by the boundary value problem

$$\Phi\Phi'' = -2\hat{F}, \quad \Phi(0) = \Phi(1) = 0, \tag{3.1}$$

where here a prime denotes differentiation with respect to H. In this section we first examine the exchange flows in two important regimes, namely, a wide channel ($B \gg 1$) and a narrow channel ($B \ll 1$), before treating channels of arbitrary width ($B = O(1)$).

1. Wide channels, B ≫ 1

In this regime the flow fields U_1 and U_2 are only dependent upon the dimensionless vertical coordinate, Z and so the governing equations may be readily integrated to deduce the form of the

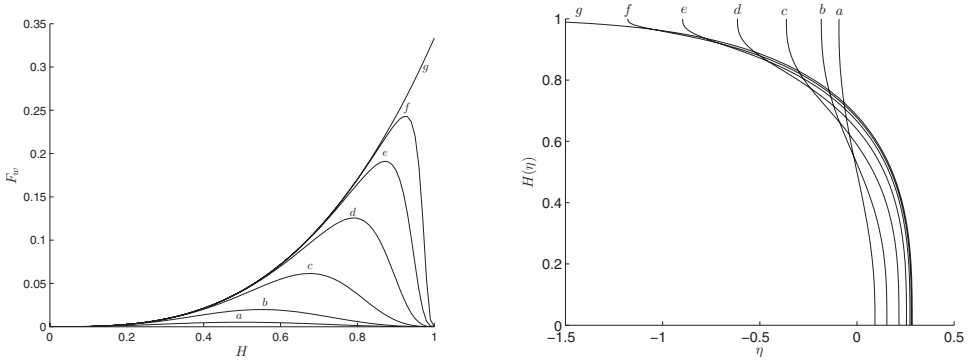

FIG. 2. (i) The flux per unit width, F_w, as a function of the height of the lower layer and (ii) the height of the interface between the fluids of differing densities, $H(\eta)$, as a function of the similarity variable η for wide channels ($B \gg 1$). Profiles are shown for various values of the viscosity ratio: (a) $r = 1$; (b) $r = 10^{-1}$; (c) $r = 10^{-2}$; (d) $r = 10^{-3}$; (e) $r = 10^{-4}$; (f) $r = 10^{-5}$; and (g) $r = 0$.

dimensionless pressure gradient

$$\frac{\partial P_t}{\partial X} = -\frac{\partial H}{\partial X}\frac{rH^2\left((1-H)(3+H)+rH^2\right)}{(1-H)^4+r(1-H^4-(1-H)^4)+r^2H^4}, \tag{3.2}$$

so that the flux function is given by

$$\hat{F} \equiv F_w = \frac{H^3(1-H)^3(1-(1-r)H)}{3((1-r)(1-H)^4+r(1-(1-r)H^4))} \tag{3.3}$$

(see Taghavi *et al.*[1] for details of this derivation). We note that in the limit of vanishing viscosity in the upper layer ($r \to 0$), $F_w \to H^3/3$, which recovers the expression used to model single layer, density-driven gravity currents.[20,21]

We plot the results for the shape of interface in terms of the similarity variable for various values of the viscosity ratio, r, in the range $r \leq 1$ (Figure 2). We note that if the fluids have identical viscosities ($r = 1$) then the interface is symmetric ($H(\eta) + H(-\eta) = 1$); this result follows immediately from the symmetries of the problem. The profiles, shown in Figure 2, have the same generic shape; they are "blunt"-nosed at the upper and lower boundaries and vary smoothly between these contact points. In the regime $r \ll 1$ the solutions for the shape of the interface within the interior of the flow approach the profile associated with the limiting case of a vanishing viscosity of the upper fluid ($r = 0$) and differ only close to the upper boundary. We note that the case $r = 0$ has to be computed carefully because $\Phi'(1) \equiv \eta_t \to -\infty$ as $r \to 0$ (cf. Gratton and Minotti[21]).

In Figure 3, we plot the variation of the upper and lower points of contact, η_t and η_b, with the viscosity ratio, r. We note the strong variation of η_t but that η_b is approximately constant. This variation may be deduced asymptotically. First, we set $r = \epsilon \ll 1$ and observe that

$$F_w(H,\epsilon) = \frac{H^3}{3}\left[1+\epsilon\,\frac{(1-H)^3-1+H^4}{(1-H)^4}+O(\epsilon^2)\right]. \tag{3.4}$$

By neglecting terms of order ϵ and introducing $\Phi = \Phi_0 + \ldots$ into Eq. (3.1), we obtain the following differential equation that governs the shape of the interface in the interior of the domain, away from the boundary at $H = 1$,

$$\Phi_0\frac{\mathrm{d}^2\Phi_0}{\mathrm{d}H^2} = -\frac{2}{3}H^3. \tag{3.5}$$

However, this approximation becomes invalid when the first two terms of Eq. (3.4) are comparable

$$\frac{(1-H)^4}{(1-H)^3-1+H^4} \sim \epsilon\,, \tag{3.6}$$

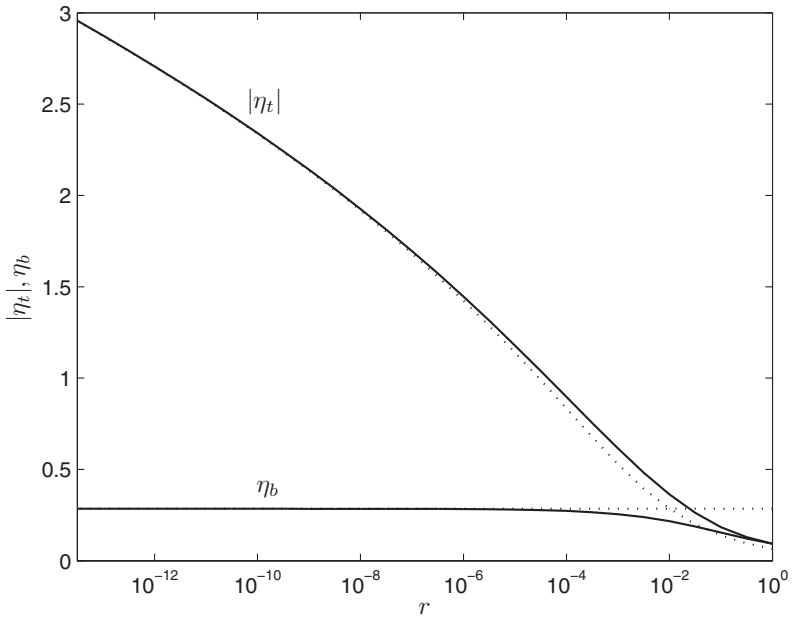

FIG. 3. The points at which the interface between the two fluids intersect the upper and lower boundaries, η_t and η_b, respectively, as a function of the ratio of the viscosities, r for wide channels ($B \gg 1$). The numerical and asymptotic results are plotted with solid and dashed lines, respectively.

which occurs when $1 - H \sim \epsilon^{1/3}$. This scaling elucidates the extent of the region close to the upper boundary within which the interface profiles diverge as r varies and demonstrates that away from this boundary the interface is given by Φ_0 to leading order. This "boundary layer" may be seen in Figure 2.

We now develop a matched asymptotic expansion to construct the interface profile and to establish how η_t and η_b depend on r. We match between an "inner" region, close to the upper boundary and the "outer" region in the bulk of the domain, within which the behaviour is governed by Eq. (3.5). We examine the behaviour within the "inner" region by writing $H = 1 - \epsilon^{1/3} Y$ and $\Phi(H) = \epsilon^{1/3}\phi_0(Y) + \ldots$ to find that to leading order

$$\phi_0 \frac{\mathrm{d}^2\phi_0}{\mathrm{d}Y^2} = -\frac{2}{3}\frac{Y^3}{Y^3+4}. \tag{3.7}$$

This equation is solved subject to $\phi_0(0) = 0$ and is matched to the outer solution as $Y \to \infty$. In terms of these variables, $\eta_t = -\mathrm{d}\phi_0/\mathrm{d}Y(0)$.

The outer solution is governed by Eq. (3.5), which may be integrated numerically subject to $\Phi_0(0) = 0$. A second boundary conditions emerges from matching to the inner solution; thus the solution at $O(1)$ satisfies $\Phi_0(1) = 0$, because any other choice would render the matching impossible. Thence, we find by numerical integration that $\eta_b = 0.2843$. We also find that Eq. (3.5) may be rewritten

$$\left(\frac{\mathrm{d}\Phi_0}{\mathrm{d}H}\right)^2 + \frac{4}{3}\log\Phi_0 = c - \frac{4}{3}\int_H^1 \frac{\mathrm{d}\log\Phi_0}{\mathrm{d}s}(1-s^3)\,\mathrm{d}s, \tag{3.8}$$

where $c = -3.0249$. Substituting $H = 1 - \epsilon^{1/3}Y$ and expanding to $O(1)$, we deduce that

$$\frac{1}{\epsilon^{2/3}}\left(\frac{\mathrm{d}\Phi_0}{\mathrm{d}Y}\right)^2 + \frac{4}{3}\log\Phi_0 = c, \tag{3.9}$$

and this will be employed below as the asymptotic matching condition.

Turning then to the "inner" solution, we first introduce $\phi_0 = |\eta_t|\varphi$ and construct the solution using a regular perturbation series by writing $\varphi = \varphi_0 + \varphi_1/\eta_t^2 + \ldots$, on the assumption that

$|\eta_t| \gg 1$. This step yields

$$\varphi_0 \frac{\mathrm{d}^2\varphi_0}{\mathrm{d}Y^2} + \frac{1}{\eta_t^2}\left(\varphi_0 \frac{\mathrm{d}^2\varphi_1}{\mathrm{d}Y^2} + \varphi_1 \frac{\mathrm{d}^2\varphi_0}{\mathrm{d}Y^2}\right) + \ldots = \frac{-2}{3\eta_t^2}\frac{Y^3}{Y^3+4}, \tag{3.10}$$

with boundary conditions at $Y = 0$ given by

$$\varphi_0(0) = 0, \quad \frac{\mathrm{d}\varphi_0}{\mathrm{d}Y}(0) = 1 \qquad \text{and} \qquad \varphi_1(0) = 0, \quad \frac{\mathrm{d}\varphi_1}{\mathrm{d}Y}(0) = 0. \tag{3.11}$$

Equating powers of $1/\eta_t^2$ it is possible to establish

$$\varphi_0 = Y \quad \text{and} \quad \varphi_1 = -\frac{2}{9}\int_0^Y \log\left(1 + \frac{s^3}{4}\right)\,\mathrm{d}s. \tag{3.12}$$

Then, matching to the "outer" solution (3.9), expanded to $O(1)$, gives

$$\lim_{Y\to\infty}\left(\eta_t^2\left(\frac{\mathrm{d}\varphi}{\mathrm{d}Y}\right)^2 + 4\log\left(|\eta_t|\epsilon^{1/3}\varphi\right)\right) = c. \tag{3.13}$$

Substituting for φ, truncated at $O(\eta_t^{-2})$, gives

$$\eta_t^2 + \frac{4}{3}\log|\eta_t| = c - \frac{4}{9}\log(4\epsilon). \tag{3.14}$$

Finally, we solve this algebraic equation numerically to determine $|\eta_t|$ as a function of the viscosity ratio $r \equiv \epsilon$ in the regime $r \ll 1$. We note that the asymptotic estimates compare favourably with numerical data, even at relatively large viscosity ratios (Figure 3).

2. *Narrow channels, B ≪ 1*

In this regime, the dominant shear in the velocity field occurs across the width of the channel. Thus, the velocity fields are dependent only on the lateral coordinate Y to leading order and are given by

$$U_1 = -\left(\frac{\partial P_T}{\partial X} + \frac{\partial H}{\partial X}\right)\frac{Y(B-Y)}{2} \qquad \text{and} \qquad U_2 = -\frac{\partial P_T}{\partial X}\frac{Y(B-Y)}{2}. \tag{3.15}$$

Equating the volume flux of fluid carried in each layer ($Q_1 + Q_2 = 0$) permits the flux to be evaluated as

$$Q_1 = -\frac{B^3 H(1-H)}{12(1-H(1-r))}\frac{\partial H}{\partial X}, \tag{3.16}$$

and thus $\hat{F} \equiv F_p = B^2 H(1-H)/[12(1-H(1-r))]$.

We note that the flow in this regime is analogous to a density-driven exchange flow within a porous layer, bounded by impermeable horizontal surfaces, with dimensionless permeability given by $B^2/12$. Such flows were analysed by Huppert and Woods[25] when the viscosities of the two fluids were equal ($r = 1$) and the study was extended by Hesse *et al.*[23] to situations in which the viscosities differed. Indeed Hesse *et al.*[23] established similarity solutions for the shape of the interface for an arbitrary ratio of the viscosities and empirically fitted functions to the numerical data to produce relationships between the points at which the interface meets the upper and lower boundaries, η_t and η_b, and the viscosity ratio, $r = \mu_2/\mu_1$ in the regime $r \ll 1$. Here we derive these relationships as a result of asymptotic analysis and find results that are broadly consistent with those of Hesse *et al.*[23] within the range over which the curves were fitted, but differ substantially outside of that regime.

The similarity function satisfies

$$\Phi\Phi'' = -\frac{B^2 H(1-H)}{6(1-H(1-r))}, \qquad \text{subject to} \quad \Phi(0) = \Phi(1) = 0. \tag{3.17}$$

For equal viscosity fluids, $\Phi = BH(1-H)/\sqrt{12}$. This yields the symmetric linear profile $H = (1 - \sqrt{12}\eta/B)/2$, as established by Huppert and Woods.[25] We plot the form of the similarity solution and the dependence of η_t and η_b in Figures 4 and 5. We note that the profiles approach

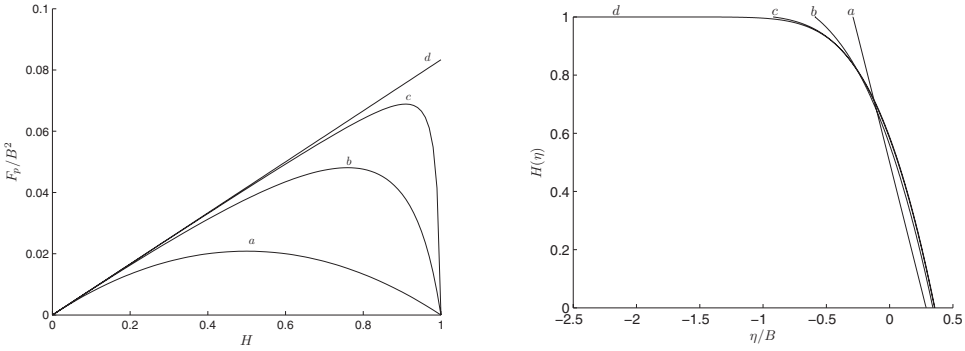

FIG. 4. (i) The flux per unit width, F_p, as a function of the height of the lower layer and (ii) the height of the interface between the fluids of differing densities, $H(\eta)$, as a function of the similarity variable η for narrow channels ($B \ll 1$). Profiles are shown for various values of the viscosity ratio: (a) $r = 1$; (b) $r = 10^{-1}$; (c) $r = 10^{-2}$; and (d) $r = 0$.

the limiting case $r = 0$ within the interior as the viscosity ratio decreases, but that they differ close to the upper boundary. As in Sec. III A, we may examine the asymptotic dependence of η_t and η_b on r in the regime $r = \epsilon \ll 1$ by noting that

$$F_p(H, \epsilon) = \frac{B^2 H}{12}\left[1 - \epsilon\,\frac{H}{1-H}\right] + O(\epsilon^2)\,. \tag{3.18}$$

We neglect terms of order ϵ and write $\Phi = B\Phi_0 + \ldots$ to find that

$$\Phi_0 \frac{\mathrm{d}^2\Phi_0}{\mathrm{d}H^2} = -\frac{H}{6}\,. \tag{3.19}$$

This approximation becomes invalid when $1 - H = O(\epsilon)$, thus we expect a "boundary layer" of $O(\epsilon)$, adjacent to the upper boundary. Within this "inner" region we substitute $H = 1 - \epsilon Y$ and

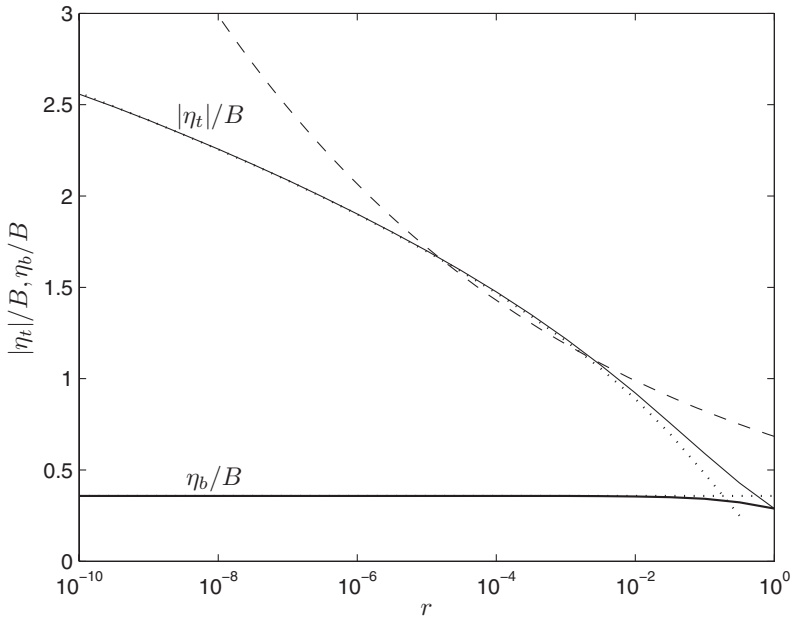

FIG. 5. The points at which the interface between the two fluids intersect the upper and lower boundaries, η_t and η_b, respectively, as a function of the ratio of the viscosities, r for narrow channels ($B \ll 1$). The numerical and asymptotic results are plotted with solid and dashed lines, respectively. Also shown is the empirical fit (dashed line) due to Hesse *et al.*[23]

$\Phi = \epsilon B\phi_0 + \ldots$ to obtain

$$\phi_0 \frac{\mathrm{d}^2\phi_0}{\mathrm{d}Y^2} = -\frac{1}{6}\frac{Y}{Y+1} \tag{3.20}$$

subject to $\phi_0(0) = 0$.

First, we integrate Eq. (3.19), subject to the boundary condition $\Phi_0(0) = 0$ with the matching condition that $\Phi_0(1) = 0$ to find that $\eta_b/B \equiv \Phi_0'(0) = 0.3575$ and that

$$\Phi_0'^2 + \frac{1}{3}\log\Phi_0 = c_1 - \frac{1}{3}\int_H^1 (1-s)\frac{\mathrm{d}}{\mathrm{d}s}(\log\Phi_0)\,\mathrm{d}s, \tag{3.21}$$

where $c_1 = -0.7839$. Then treating the "inner" region by substituting $\phi_0 = |\eta_t|\varphi/B$ and expanding in powers of $B/|\eta_t|$, we find that

$$\varphi = Y + \frac{B^2}{6\eta_t^2}\left(Y - (Y+1)\log(Y+1)\right) + \ldots \tag{3.22}$$

Finally, matching to the outer solution (3.21), we find that

$$\left(\frac{\eta_t}{B}\right)^2 + \frac{1}{3}\log\left|\frac{\eta_t}{B}\right| = c_1 - \frac{1}{3}\log\epsilon\,. \tag{3.23}$$

This algebraic equation may be solved numerically to obtain an estimate for η_t as r tends to zero. The result is plotted in Figure 5, where we observe that the numerical data is very well represented by the asymptotic result.

We compare these asymptotic results with the scaling laws fitted by Hesse *et al.*[23] In the regime $r \ll 1$, we have shown that to leading order $\eta_b/B = 0.3575$, while Hesse *et al.*[23] propose empirically that $\eta_b/B = 0.3580$. The other contact point, η_t, is given by the solution of Eq. (3.23). In contrast Hesse *et al.*[23] propose that $|\eta_t|/B = 2.37r^{-0.08}/\sqrt{12}$ for $r < 0.005$. While this empirical fit is reasonably close to the numerical and asymptotic results for the regime in which it was derived ($10^{-4} < r < 10^{-2}$), it diverges as r is further reduced.

3. Arbitrary width channels B = O(1)

When the width of the channel is of order unity, the velocity fields, U_1 and U_2 now depend upon both the lateral and vertical coordinates. They may be calculated by a straightforward, though lengthy, calculation using separable solutions (see, for example, Batchelor[28] for the solution for a single fluid within a channel). Thus we find that

$$U_1 = \frac{1}{2}\frac{\partial(P_t+H)}{\partial X}Y(Y-B) + \sum_{m=0}^{\infty}\frac{4B^2}{(2m+1)^3\pi^3}\left(A_m\sin\left(\frac{(2m+1)\pi Y}{B}\right)\sinh\left(\frac{(2m+1)\pi Z}{B}\right)\right.$$
$$\left. + \frac{\partial(P_t+H)}{\partial X}\sin\left(\frac{(2m+1)\pi Y}{B}\right)\cosh\left(\frac{(2m+1)\pi Z}{B}\right)\right), \tag{3.24}$$

$$U_2 = \frac{1}{2r}\frac{\partial P_t}{\partial X}Y(Y-B) + \sum_{m=0}^{\infty}\frac{4B^2}{(2m+1)^3\pi^3}\left(C_m\sin\left(\frac{(2m+1)\pi Y}{B}\right)\sinh\left(\frac{(2m+1)\pi(1-Z)}{B}\right)\right.$$
$$\left. + \frac{1}{r}\frac{\partial P_t}{\partial X}\sin\left(\frac{(2m+1)\pi Y}{B}\right)\cosh\left(\frac{(2m+1)\pi(1-Z)}{B}\right)\right), \tag{3.25}$$

where the constants A_m and C_m are determined by imposing the continuity of velocity and shear stress at the interface between the fluids. This yields

$$A_m = -\frac{\partial P_t}{\partial X}f(\chi,\chi^*,r) - \frac{\partial(P_t+H)}{\partial X}g(\chi,\chi^*,r), \tag{3.26}$$

$$C_m = -\frac{1}{r}\frac{\partial P_t}{\partial X}g(\chi^*,\chi,1/r) - \frac{1}{r}\frac{\partial(P_t+H)}{\partial X}f(\chi^*,\chi,1/r), \tag{3.27}$$

with $\chi = (2m+1)\pi H/B$, $\chi^* = (2m+1)\pi(1-H)/B$ and

$$f = \frac{\cosh\chi^* - 1}{\cosh\chi\,\sinh\chi^* + r\cosh\chi^*\sinh\chi} \quad \text{and} \quad g = \frac{\sinh\chi\,\sinh\chi^* - r\cosh\chi^*(1-\cosh\chi)}{\cosh\chi\,\sinh\chi^* + r\cosh\chi^*\sinh\chi}. \tag{3.28}$$

From these expression we may integrate across the channel to find the volume flux of fluid carried in each layer. Then, from the balance of volume fluxes ($Q_1 + Q_2 = 0$), we find that

$$\frac{\partial P_t}{\partial X} = -\frac{G_1}{G_1+G_2}\frac{\partial H}{\partial X}, \tag{3.29}$$

where

$$G_1 = \frac{B^2 H}{12} + \sum_{m=0}^{\infty}\frac{8B^3}{(2m+1)^5\pi^5}\left(-\sinh\chi + (\cosh\chi - 1)g(\chi,\chi^*,r) + \frac{(\cosh\chi^*-1)}{r}f(\chi^*,\chi,\frac{1}{r})\right), \tag{3.30}$$

$$G_2 = \frac{B^2(1-H)}{12r} + \sum_{m=0}^{\infty}\frac{8B^3}{(2m+1)^5\pi^5}\left(-\frac{\sinh\chi^*}{r} + (\cosh\chi - 1)f(\chi,\chi^*,r) + \frac{(\cosh\chi^* - 1)}{r}g(\chi^*,\chi,\frac{1}{r})\right). \tag{3.31}$$

Finally, we may combine these expressions to find the flux in the lower layer,

$$Q_1 = -\frac{B}{G_1+G_2}\frac{\partial H}{\partial X}\left(\frac{B^2 H}{12}G_2 - G_2\sum_{m=0}^{\infty}\frac{8B^3}{(2m+1)^5\pi^5}\left(\sinh\chi - (\cosh\chi - 1)g(\chi,\chi^*,r)\right) - G_1\sum_{m=0}^{\infty}\frac{8B^3}{(2m+1)^5\pi^5}(\cosh\chi - 1)f(\chi,\chi^*,r)\right). \tag{3.32}$$

Denoting $Q_1 = -F_{2D}B\frac{\partial H}{\partial X}$, we may identify $\hat{F} = F_{2D}$, which can be evaluated numerically by truncating the series expansions at a term to ensure sufficient convergence. (In this study the series were truncated after 100 terms.) The dependence of F_{2D} on the height of the interface when the viscosities are equal ($r = 1$) is plotted in Figure 6 for a range of dimensionless channel widths. We note that in the regimes of wide ($B \gg 1$) and narrow ($B \ll 1$) geometries that this expression reduces to the forms presented in the preceding sections. Furthermore, we note that these profiles

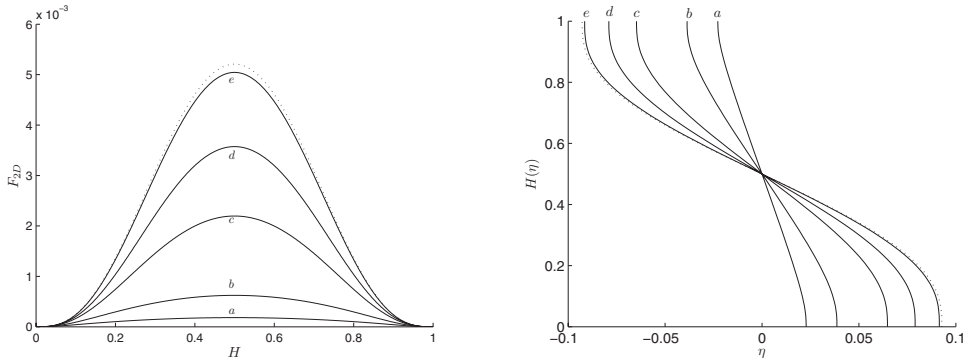

FIG. 6. (i) The volume flux of fluid carried in the lower layer, F_{2D} as a function of interface height and (ii) The interface between the two fluids, $H(\eta)$ as a function of the similarity variable, η, when the viscosities of the two fluids are identical ($r = 1$) for dimensionless channel widths: (a) $B = 0.1$; (b) $B = 0.2$; (c) $B = 0.5$; (d) $B = 1$; (e) $B = 10$. Also plotted is the flux and interface for a wide channel (dotted line, $B \to \infty$).

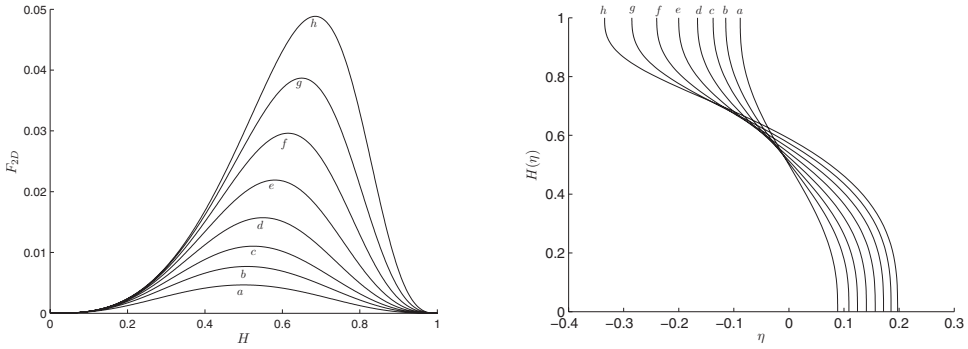

FIG. 7. (i) The volume flux of fluid carried in the lower layer, F_{2D}, as a function of interface height and (ii) the interface between the two fluids, $H(\eta)$, as a function of the similarity variable, η, when the aspect ratio $B = 3$ for various ratios of viscosities: (a) $r = 1$; (b) $r = 10^{-6/15}$; (c) $r = 10^{-10/15}$; (d) $r = 10^{-14/15}$; (e) $r = 10^{-18/15}$; (f) $r = 10^{-22/15}$; (g) $r = 10^{-26/15}$; and (h) $r = 10^{-30/15}$.

are symmetric about the midline ($H = 1/2$), as anticipated. In Figure 7, we plot the flux as a function of the height of the interface when $B = 3$ for a range of viscosity ratios. We note that decreasing the viscosity ratio, r, makes the flux function increasingly asymmetric.

We now use the expression for the flux to compute the similarity solution for the shape of the interface between the two fluids, by numerically integrating the boundary value problem with $\hat{F} = F_{2D}$. In Figure 6 we plot some profiles when the fluids have equal viscosities ($r = 1$); these are symmetric due to the underlying symmetry of the flux function. Also when $B > 10$, the form of the interface is quite close to that found for wide channels ($B \gg 1$). We plot the front position, η_b as a function of the channel width in Figure 8. These results illustrate η_b is an increasing function of the channel width and that in the regimes $B \gg 1$ and $B \ll 1$, the respective asymptotic results $\eta_b = 0.0928$ and $\eta_b = 0.2887B$ are attained (these asymptotic estimates concur with those derived by Refs. 1, 18, and 25). We note that the effects of the channel width remain appreciable for relatively large B; for instance, the predicted position of the front, η_b, remains 1.3% less than the wide channel

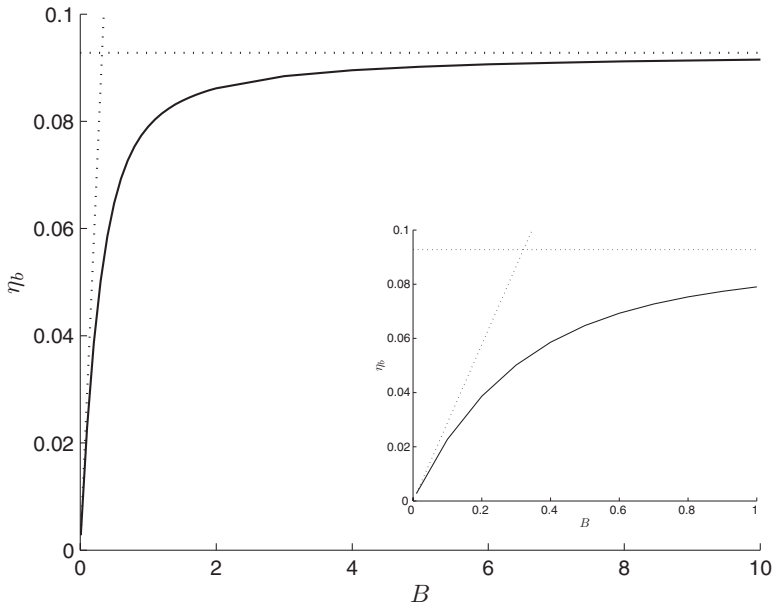

FIG. 8. The lower contact point, η_b for exchange flows of equal viscosity fluids ($r = 1$) as a function of dimensionless channel width, B. Also shown with dotted lines are the results for narrow ($B \ll 1$) and wide channels ($B \gg 1$). The inset figure shows the same data over an expanded range.

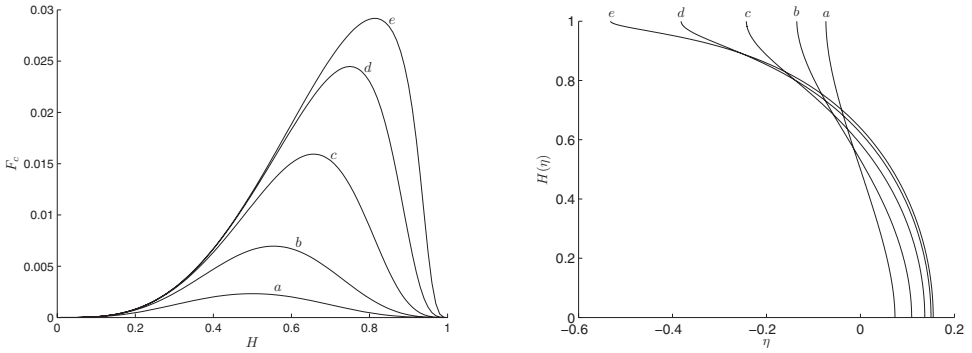

FIG. 9. (i) The dimensionless volume flux of fluid carried in the lower layer, $F_c = -Q_1/(\partial H/\partial X)$, as a function of the height of the interface and (ii) the interface between the two fluids, $H(\eta)$ as a function of the similarity variable, η for exchange flow in a pipe of circular cross section for a range of viscosity ratios: (a) $r = 1$; (b) $r = 2^{-3}$; (c) $r = 2^{-6}$; (d) $r = 2^{-9}$; and (e) $r = 2^{-12}$.

result even when $B = 10$. The results for $B = 3$ and a varying viscosity ratio are presented in Figure 14, since these correspond to the experimental configuration (Sec. IV). The results illustrate the asymmetrical spreading that occurs when the viscosities are not equal; in particular we observe that when $r \ll 1$, the more viscous fluid spreads more slowly than the less viscous fluid.

B. Pipes of circular cross section

Density-driven exchange flows along pipes with circular cross sections are modelled by assuming that the interface between the fluids remains invariant of the horizontal axis perpendicular to the axis along the pipe, an assumption, which is valid, provided the surface tension remains negligible. Thus, using the diameter of the pipe as the lengthscale with which to render the variables and equations dimensionless, the area below the interface is given by $A(H) = (\cos^{-1}(1 - 2H) - 2(1 - 2H)H^{1/2}(1 - H)^{1/2})/4$ and thus $\mathrm{d}A/\mathrm{d}H = 2H^{1/2}(1 - H)^{1/2}$.

The flow fields are calculated using the methods developed by Kerswell[16] and in this way the flux function, F_c, is determined. The particular problem under consideration here is a specific case of more general bidirectional steady flows within a pipe of circular cross section treated by Kerswell.[16] Here the interface between the fluids is flat, because surface tension is neglected and due to the orientation of the axis of the tube, the dense fluid always forms a single connected region below this interface. The volume flux in each layer is calculated following the methods of Kerswell:[16] both regions within the pipe are conformally mapped into half planes and then the velocity field is readily constructed. The calculation of the flux function, F_c, typically requires the numerical evaluation of triple integrals. The parameterisation used by Kerswell[16] to evaluate the integrals is formally singular when the interface is flat, but this limit is regular and so may be evaluated without special attention. We note that the special case of an interface at $H = 1/2$ can be handled much more simply (see, for example, Packham and Shail[9]) and this provides a valuable check on the numerical output from the more general problem. Also the flux functions, F_c, can be deduced asymptotically in the regimes $H \ll 1$ ($F_c = -\frac{32}{105}H^{7/2} + \ldots$) and $1 - H \ll 1$ ($F_c = -\frac{32}{105r}(1 - H)^{7/2} + \ldots$); these results provide further checks on the computations.

We plot the dimensionless flux function, F_c, for a range of viscosity ratios in Figure 9, noting the symmetry about $H = 1/2$ when $r = 1$. (For this case of equal viscosities, Seon *et al.*[17] suggest empirically that $F_c \approx \frac{32}{105}(H(1 - H))^{7/2}$, which fits the exact result sufficiently closely that the two are indistinguishable in Figure 9.) As the viscosity ratio is reduced, these flux functions become asymmetric about the centre line ($H = 1/2$) and approach each other provided the interface is not close to the top of the pipe. Such an asymmetry is reflected in the interface profiles (Figure 9). Finally, we analyse the variation of the locations at which the interface contacts the uppermost and lowermost points of the tube boundary, η_t and η_b, respectively, noting that these are only a function of the ratio of viscosities, r (Figure 10).

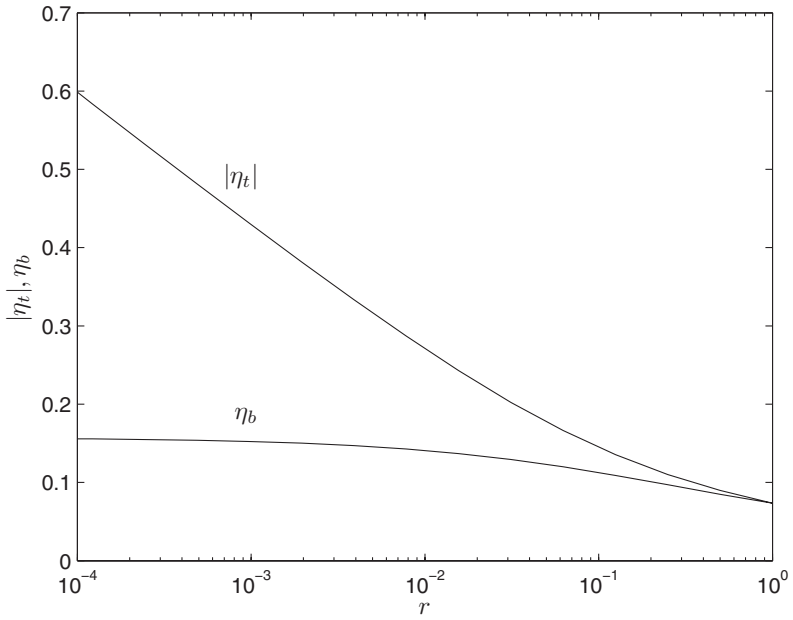

FIG. 10. The points at which the interface contacts the top of the pipe, η_t and the bottom of the pipe, η_b as a function of the viscosity ratio, r.

IV. EXPERIMENTS

We investigated density-driven viscous exchange flows experimentally in a closed, perspex channel of height 4 cm, width 12 cm, and length 100 cm. At the midpoint of the tank, a lock gate was inserted to separate the two fluids initially. At the far ends of each side on the top surface are cylindrical openings into the tank, through which fluid was added. These openings permit a slight excess of fluid to be added in order to fill the void formed when the lock gate is removed. Considerable care was taken to maintain equal levels on both sides of the tank so as not to cause an external pressure difference on the system.

The fluid used in all the experiments was golden syrup (Tate & Lyle Ltd), which exhibits an approximate Newtonian rheology[14] and is miscible with water. The water solubility enabled us to generate fluids of different densities and viscosities. Pure syrup has a viscosity of approximately 60 Pa s at 20 °C and density of 1450 kg m^{-3}. Adding a small amount of water to syrup results in a dramatic reduction in the viscosity. For example, a mixture composed of 95% syrup and 5% water has a viscosity approximately 11 Pa s and a mixture of 90% syrup and 10% water has viscosity approximately 3.5 Pa s. The densities of such mixtures, however, change approximately linearly with water content.

In all experiments two different syrup-water mixtures were made up. The different proportions of water not only alter the viscosity but also provided a density difference to drive the flows. In some experiments salt (sodium chloride) was added to the less dense fluid in order to increase its density and hence reduce the driving force to ensure inertial effects could be neglected after a relatively short period following initiation. Food dye was then added to one fluid in order that the interface could easily be viewed. The density of the fluid was determined using a 250 cm^3 volumetric (narrow necked) flask and a balance accurate to 0.001 g. The viscosity was measured using a Haake rotary viscometer.

The two fluids were added to either side of the lock gate and left to settle for 5 min in order for any residual motion to dissipate. The lock gate was then rapidly removed and digital photos taken of the flow at regular intervals to record the interface profile. Several experimental runs were also recorded using a digital video camera. Each experiment was stopped once the fronts near the ends of the tank.

TABLE I. Experimental details.

Expt.	Fluid 1		Fluid 2			
	μ_1 (Pa s)	ρ_1 (kg m^{-3})	μ_2 (Pa s)	ρ_2 (kg m^{-3})	$\Delta\rho$ (kg m^{-3})	$r = \mu_2/\mu_1$
1	55.2	1422.9	9.0	1403.2	19.7	0.16
2	9.4	1406.2	1.8	1385.0	21.2	0.19
3	7.9	1412.8	0.4	1360.4	52.4	0.04
4	5.4	1405.2	5.2	1398.8	6.4	0.96
5	8.1	1411.0	1.9	1395.4	15.6	0.23
6	3.2	1410.2	0.8	1383.4	26.8	0.23
7	48.2	1451.4	0.9	1387.9	63.5	0.02
8	7.0	1415.1	0.8	1388.6	26.5	0.12
9	1.9	1405.2	4.0	1403.0	3.2	2.07
10	9.8	1420.8	0.7	1375.3	45.5	0.07
11	13.0	1418.5	1.4	1389.4	29.1	0.11
12	10.4	1418.6	1.2	1375.8	42.8	0.11

It was difficult to eliminate all the bubbles from the fluids. Bubbles were both entrained during the filling process and formed where air pockets became trapped at the upper boundary. No method could be identified to prevent completely the entrainment of bubbles but the filling method was modified to minimise the trapped air bubbles. The apparatus was inclined at an angle of approximately 5° during filling, which forced the air pocket to be trapped at the lock gate in the lower fluid and in the top corner of the upper fluid. The lock gate was not completely air tight and additionally a small tube was inserted into the upper pocket to allow this air to escape.

All the results were measured from the digital still images and in general it was possible to measure lengths with an accuracy of ±0.25 mm. It is estimated that densities are measured with an accuracy of ±0.5 kg m^{-3}, yielding an error in the relative density difference, $\Delta\rho/\rho$ of between 1%–10%. The viscosities estimated from the viscometer measurements exhibited weak dependence on the applied strain rates. The mean viscosity was used in calculations and the standard deviation of the measurements, used as an estimate of the error, is typically between 5%–10% of the mean.

A. Results

The conditions for each of the experimental runs are listed in Table I, while typical images are given in Figure 11. Using the similarity scaling, $\eta = X/\sqrt{T}$, and reinserting dimensions yields an equation governing the rate of spreading,

$$x = \eta(H, r)\sqrt{\frac{\Delta\rho g d^3}{\mu_1}}\sqrt{t}\,. \tag{4.1}$$

For each experiment we scale profiles into similarity form at each time to compare with the predicted profiles of Sec. III (see, for example, Figures 12 and 13). We estimate that the error in the determination of η lies in the range 3%–10% of the measured value. To examine Eq. (4.1), we plot the positions of the interface at the upper and lower boundaries, $x_t(t)$ and $x_b(t)$, respectively, as functions of time (see, for example, Figures 12 and 13).

During propagation, the front was quasi two-dimensional with the only deviation occurring at the side walls due to no-slip there (Figure 11). These boundary layers were typically about 1 cm in extent and hence more than 80% of the flow occurred outside of them. Striations parallel to the direction of flow are observed and interpreted as gravitationally driven descent of relatively dense, un-dyed fluid through the less dense intruding fluid.[29] As illustrated by photographs of the interface (Figure 11), the effect of the no-slip boundary condition is to have relatively dense fluid override less dense fluid at the lower boundary and vice versa at the upper boundary. The over(under)-ridden fluid is gravitational unstable and ascends (descends) through the intruding flow. It is noteworthy

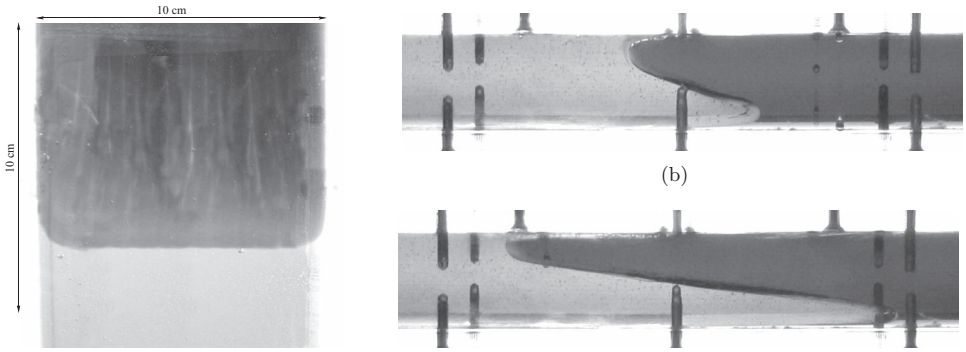

FIG. 11. (a) Photograph of the interface between the fluids (experiment 4), viewed from above the tank and looking down onto the flow. This image was taken 2400 s after release, by which stage the front had moved 12.2 cm from the lock gate. (b,c) Images of experiment 11 after (b) 60 s and (c) 300 s.

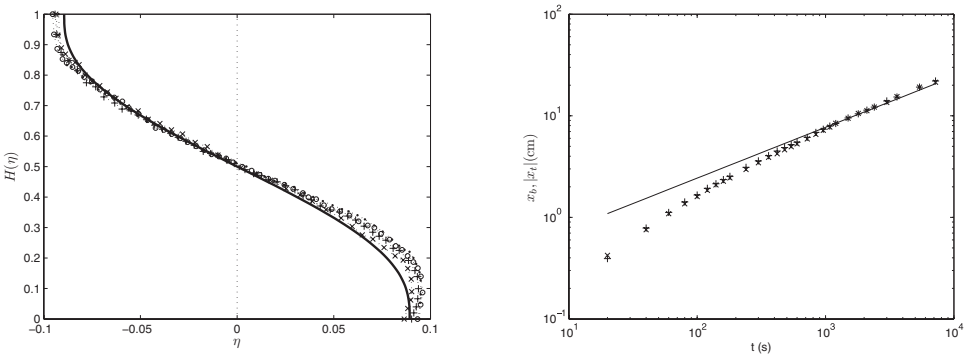

FIG. 12. Results for experiment 4 with viscosity ratio $r = 0.96$. (a) The height of the interface, $H(\eta)$, as a function of the similarity variable η at $t = 1800$ s ($- \times -$); $t = 3600$ s ($- + -$); $t = 5400$ s ($- \circ -$); and $t = 7200$ s ($- \bullet -$). The theoretical curve is also plotted (—). (b) The position of the interface at the upper and lower boundaries, $|x_t|$ ($\times$) and x_b ($+$), respectively, as a function of time. Also plotted are the theoretical predictions, $|x_t|$ (- -) and x_b (—) although the two curves are indistinguishable in this plot.

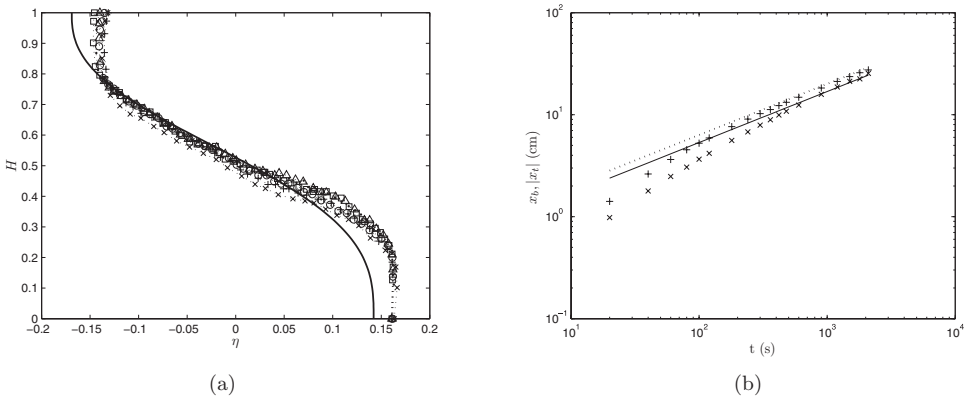

FIG. 13. Results for experiment 11 with viscosity ratio $r = 0.11$. (a) The height of the interface, $H(\eta)$, as a function of the similarity variable η at $t = 300$ s ($- \times -$); $t = 600$ s ($- + -$); $t = 900$ s ($- \circ -$); $t = 1200$ s ($- \bullet -$); $t = 1500$ s ($- \square -$); and $t = 1800$ s ($- \triangle -$). The theoretical curve is also plotted (—). (b) The position of the interface at the upper and lower boundaries, $|x_t|$ ($\times$) and x_b ($+$), respectively, as a function of time. Also plotted are the theoretical predictions $|x_t|$ (- - -) and x_b (—).

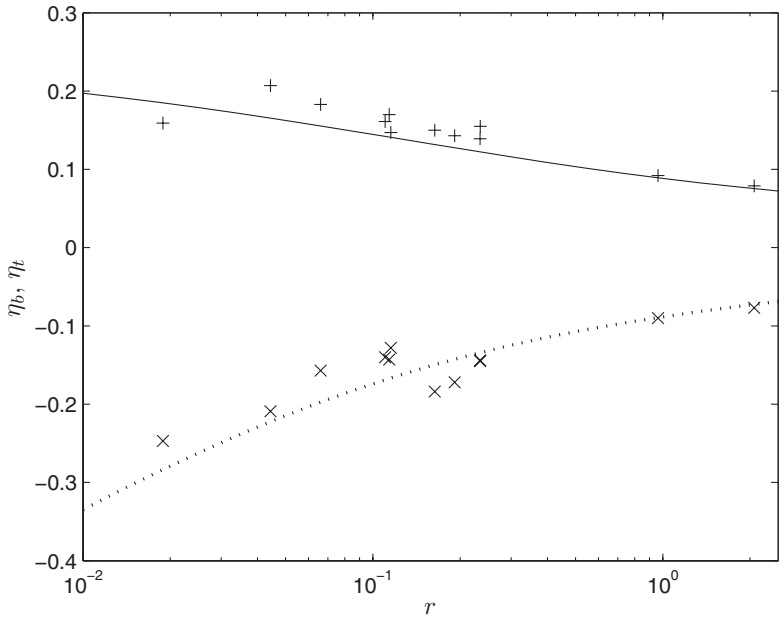

FIG. 14. The experimentally measured positions of the fronts of the interface in terms of the similarity variable, η_b (+) and η_t (×), as functions of viscosity ratio, r. Also plotted are the theoretical predictions for η_b (—) and η_t (- -).

that all images of the motion feature a relatively sharp interface between the fluids, which illustrates that diffusion is negligible on the time scales of these motions.

The results of experiment 4 are plotted in Figure 12. In this case the profiles agree extremely well with the theoretical profile. The data from the front show that initially the interface does not spread proportionally to $t^{1/2}$ as would be predicted by Eq. (4.1). This difference occurs because during the first stages of the motion the pressure is not hydrostatic and inertia is not negligible and hence insufficient time has passed for the flow to enter the regime modelled in Sec. III. However, after approximately 10 min the agreement with Eq. (4.1) becomes very good.

We next consider the results for experiment 11 in which $r = 0.11$. Snapshots of the profile are given in Figure 11 and measurements of the shape of the interface and the front position are reported in Figure 13. The agreement with theory is not as good as before although the profiles appear to be self similar. The bottom of the flow has propagated marginally further than the theoretical predictions, although they are sufficiently close that much of the difference could be accounted by experimental error. However, the top has not propagated as far as anticipated. In fact, it is shorter than the bottom whereas theory predicts the converse. This feature was present in some of the experimental runs and some possible reasons for this are discussed below. Once again we see that in the early stages of the motion the front of the flow does not spread as $t^{1/2}$ but appears to follow the similarity scaling in later stages as expected.

We collect all of the experimental data together and plot the change in the contact points at the bottom, η_b, and top, η_t, as we alter the viscosity ratio, r (Figure 14). Near $r = 1$ the agreement with theory is excellent but as r is reduced the scatter of data points increases. In five of the experiments the top did not propagate as far as the bottom, contrary to what is predicted by the theory.

B. Discussion of results

A feature of some of the experimental results when compared to theoretical predictions is that the bottom contact point agrees well with the theoretical prediction but the upper contact point does not propagate as far as expected. In many cases it actually did not move as far as the contact point at the base. There are many possible factors that could account for this difference and we discuss some of them below.

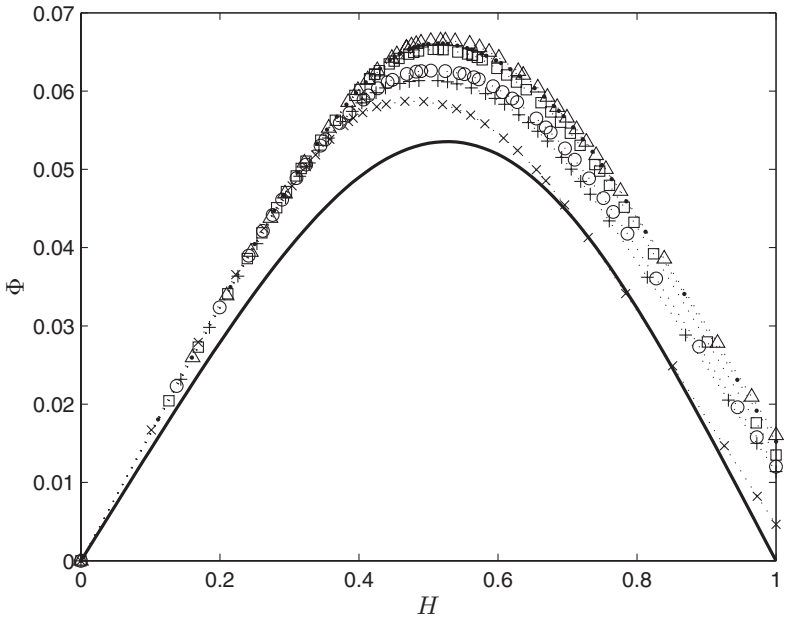

FIG. 15. The integrated similarity variable, $\Phi(H) = \int_0^H \eta(H')\mathrm{d}H'$, determined for experiment 11 at $t = 300$ s ($-\times-$); $t = 600$ s ($-+-$); $t = 900$ s ($-\circ-$); $t = 1200$ s ($-\bullet-$); $t = 1500$ s ($-\square-$); and $t = 1800$ s ($-\triangle-$). Also plotted is the theoretical prediction (—).

A first possibility is that the flows have not yet entered the similarity regime. We showed above (Sec. II) that on physical and mathematical grounds we expect the motion to approach a state in which there is a balance between viscous and gravitational forces, but that this transition decays algebraically in time. In fact, we further observed that when $r < 1$ the perturbation at the upper boundary is larger than that at the lower boundary and so we expect to have to wait longer to have good agreement with theory for the upper contact point. Careful examination of Figure 13(b) reveals that while the contact point at the base (x_b) starts spreading like $t^{1/2}$ after approximately 5 min, however, the point at the upper boundary (x_t) is still spreading at a slightly greater exponent of time even at the end of the experiment (30 min). Hence, similarity balance may not be fully attained – but this does not fully explain the observations because we see little evidence of a progressive approach to the similarity solution.

Another potential problem was the presence of bubbles, entrained as the fluids were added to the tank. Due to the high viscosity of the fluids used (the least viscous fluid was 400 times more viscous than water) the bubbles rose very slowly and it was impractical to wait for them to be expelled. A typical duration of an experiment was between 30 to 120 min and during this time entrained bubbles became concentrated towards the upper boundary and thus their accumulation will tend to enhance the viscosity of the upper fluid.[28] This process will effectively increase the viscosity ratio, r, but appears not to account fully for the differences between theory and observations.

A prominent feature of Figure 13(a) is that it seems from the one-dimensional profile that mass is not conserved within the flow. This system is investigated by reverting to the variable $\Phi(H) = \int_0^H \eta(H')\mathrm{d}H'$, for which mass conservation requires that $\Phi(1) = 0$. The similarity solution in this variable and instantaneous fluid profiles integrated across the depth are plotted in Figure 15 for experiment 11. We observe that $\Phi(1) > 0$ and hence apparently mass is not conserved within the flows and also that $\Phi(1)$ increases with increasing time. The consequence of $\Phi(1)$ being positive is that more mass has travelled in the positive x direction, the direction the denser fluid moves. This effect may be caused by an imbalance of the levels of fluid in the cylindrical opening used to fill the void when the lock gate is removed. In all experimental runs great care was taken to ensure the levels were similar but because the densities of the fluids differ even with identical

heights a small pressure difference will be imposed. With time this pressure difference could shift the effective spatial origin, possibly explaining the discrepancies observed. This observation may explain why the error is larger in experiment 11 than in experiment 4 because the density difference in experiment 11 is approximately five times larger than in experiment 4 (for which $\Phi(1) \approx 0.005$). We attempted to rectify this defect by empirically forcing mass to be conserved by adjusting the location of the spatial origin such that $\Phi(1) = 0$, which produced a small improvement in the agreement between experiment and theory, but was insufficient to account fully for the differences.

Finally, we note that another process that could account for the difference between the theory and experiments is mixing between the fluids that are over- and under-ridden at the lower and upper boundaries, respectively. As shown in Figure 11, the requirement of no-slip at the boundaries leads to the foremost parts of the flow being displaced away from the boundaries. Such an effect is not accounted for at all in the model where it is assumed that the interface varies monotonically with distance from the boundary. Fluid that is over-ridden at the lower boundary will nevertheless ascend through the domain driven by gravity while the under-ridden fluid at the upper boundary will descend. Then mixing between the fluids will alter their composition and potentially affect the rates of propagation in these exchange flows.

V. CONCLUSION

We have studied theoretically and experimentally density-driven exchange flows between fluids of differing viscosities in a two-dimensional channel. After a sufficient time following initiation, these flows become relatively long and narrow so that they adopt a hydrostatic pressure distribution and are governed by a balance between this pressure gradient and the divergence of the viscous stresses. In this regime the interface between the two fluids is governed by a similarity solution in which the intrusion rates along the upper and lower boundaries are proportional to $(\Delta\rho g d^3 t/\mu_1)^{1/2}$, where the constants of proportionality depend only on the viscosity ratio, $r = \mu_2/\mu_1$, and potentially on the geometrical characteristics of the channel, such as its aspect ratio. This time dependence is robustly observed in the experiments.

The similarity solutions are constructed by interchanging the dependent and independent variables. This technique simplifies the solution of the governing equations and enables the boundary conditions to be enforced readily. Such a change of variable is possible because the interface height varies monotonically in x. We suggest that this variable transformation may be usefully employed in other circumstances as well.[30] The shape of the interface varies systematically with the viscosity ratio, attaining a limiting form in the regime $r \ll 1$, where variation with r is only found close to the upper boundary. Solutions in this regime may be constructed using matched asymptotic expansions between the interior region and the region close to the upper boundary. The experiments show that when the viscosities of the two fluids are approximately equal, then the interface is accurately predicted by the theory. However, when the viscosities differ by an order of magnitude, although of apparently self-similar form, there are some differences between the predictions and measurements.

The similarity solutions, shown to be linearly stable, are expected to be approached from arbitrary initial conditions. These exchange flows are not driven by an imposed pressure gradient; rather they develop their own pressure distribution as the fluid intrudes. Furthermore, they are viscously dominated. Thus, many of the instabilities found in other scenarios do not arise.[6,11,12] Also an equivalent of Saffman-Taylor fingering[5] does not occur because although less viscous fluid is displacing more viscous, the pressure gradient changes sign across the interface and so the growth of disturbances is not favourable. The no-slip condition does, however, lead to the over-ride of the less dense fluid by the denser fluid at the lower boundary (and conversely at the upper boundary). This overridden fluid is gravitationally unstable and rises, leading to the striations seen the experiments. Although these appear not to affect the exponent of time in the spreading (the fronts along the upper and lower boundaries still vary as $t^{1/2}$), mixing may alter the density and viscosity differences between the fluids and potentially could account for some of the mismatch between the experimental measurements and the theoretical predictions.

ACKNOWLEDGMENTS

Richard Kerswell is thanked for the use of his numerical codes to determine the flux function of an exchange flow in a circular pipe. Howard Stone and Laurence Rongy are thanked for providing detailed comments on an earlier version of this paper.

APPENDIX: FREE-SURFACE FLOW – WIDE CHANNELS ($B \gg 1$)

We examine the density-driven exchange flow when the upper boundary is a free-surface, rather than an impermeable rigid boundary. This implies that the flow depth is potentially now variable (in dimensional form, $z = d(x, t)$), that there is vanishing shear stress at the free surface ($\partial u_2/\partial z = 0$) and that the pressure is atmospheric at this surface. Initially, the flows are of depth d_0 and this is the lengthscale that is used to render the equations dimensionless according to the definitions given in Eq. (2.5), with the addition of $D = d(x, t)/d_0$. While the flow fields could be readily calculated for any channel widths, in this subsection we derive the results only in the regime $B \gg 1$.

The dimensionless flow fields are given by

$$U_1 = \frac{1}{2}\left(\frac{\rho - \Delta\rho}{\rho}\frac{\partial D}{\partial X} + \frac{\partial H}{\partial X}\right)Z^2 - \left(\frac{\rho - \Delta\rho}{\rho}D\frac{\partial D}{\partial X} + H\frac{\partial H}{\partial X}\right)Z, \tag{A1}$$

$$U_2 = \frac{1}{r}\frac{\rho - \Delta\rho}{\rho}\frac{\partial D}{\partial X}\left(\frac{Z^2}{2} - ZD + (r-1)\left(\frac{H^2}{2} - HD\right)\right) - \frac{H^2}{2}\frac{\partial H}{\partial X}. \tag{A2}$$

These are integrated to yield the volume fluxes per unit width carried in each layer and then by balancing the fluxes, we deduce

$$\frac{\rho - \Delta\rho}{\rho}\frac{\partial D}{\partial X} = -\frac{\partial H}{\partial X}\frac{rH^2(3D - H)}{2(rD^3 + (1-r)(D-H)^3)}, \tag{A3}$$

$$Q_1 \equiv -F_s\frac{\partial H}{\partial X} = -\frac{H^3(D-H)^3(4(D-H) + 3rH)}{12((1-r)(D-H)^4 + rD^3(D-H))}\frac{\partial H}{\partial X}. \tag{A4}$$

Finally, we assume that the density difference between the fluids is small relative to the density of the fluids ($\Delta\rho/\rho \ll 1$) and thus the free-surface undergoes only small deviations from its initial state. Thus, writing $D = 1 + O(\Delta\rho/\rho)$, we find that

$$F_s = \frac{H^3(1-H)^3(4(1-H) + 3rH)}{12((1-r)(1-H)^4 + r(1-H))}. \tag{A5}$$

Free-surface flows in this configuration do not exhibit the same symmetries as those in confined channels and thus to investigate the full range of interface shapes, we must consider all values of the viscosity ratio, r.

We construct the similarity solutions for the shape of the interface between the two fluids and the profiles are plotted in Figures 16. As $r \to 0$, we note that the interface approaches that found for $r = 0$ in the interior but differs close to the upper boundary. This behaviour is reminiscent of the confined channel flow (see Sec. III A 1). As $r \to \infty$, the interface progressively approaches the limiting case throughout the entire domain. In Figure 17, we plot the variation of η_t and η_b as functions of r.

The behaviour in the regime $r \ll 1$ is captured asymptotically using a very similar approach to that derived in Sec. III. It is based upon $F_s = H^3/3 + O(\epsilon)$ when $r = \epsilon \ll 1$, an expansion that becomes invalid when $1 - H = O(\epsilon^{1/3})$. The scaling determines the extent of the boundary layer at the free-surface. Furthermore

$$F_s(1 - \epsilon^{1/3}Y) = \frac{Y^3}{3(Y^3 + 1)} + \ldots. \tag{A6}$$

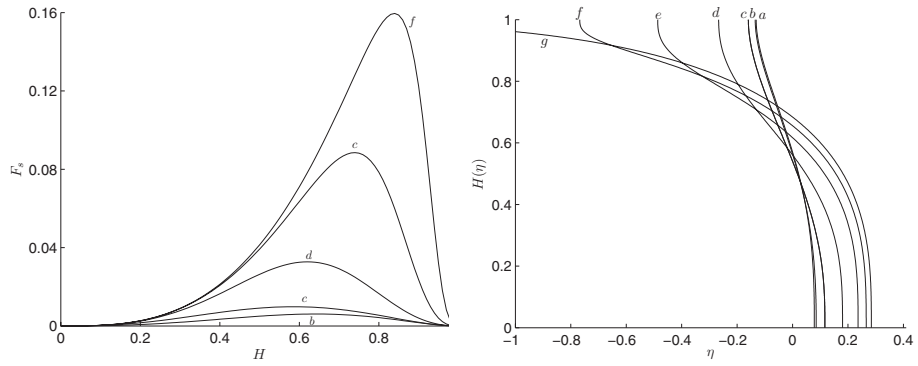

FIG. 16. (i) The volume flux per unit width, F_S, as a function of the interface height and (ii) the interface between the fluids, $H(\eta)$, as a function of the similarity variable, η, for a free-surface flow in a wide channel for various ratios of viscosities: (a) $r \to \infty$; (b) $r = 10$; (c) $r = 1$; (d) $r = 10^{-1}$; (e) $r = 10^{-2}$; (f) $r = 10^{-3}$; and (g) $r = 0$.

Then following the method of Sec. III, we deduce that $\eta_b = 0.2843$ and

$$\eta_t^2 + \frac{4}{3}\log|\eta_t| = c - \frac{4}{9}\log\epsilon, \tag{A7}$$

where $c = -3.0249$.

In the regimes $r \gg 1$ and $H \gg 1/r$, we may establish that

$$F_s = \frac{H^3(1-H)^2}{4(H^2+3(1-H))} + \ldots \tag{A8}$$

and thus we may integrate $\Phi_0''\Phi_0 = -2F_s$ to determine the profile away from the lower boundary. However, formally we may not impose the boundary condition, $\Phi_0(0) = 0$ without considering the form of F_s in the regime $1/r \gg H$ and asymptotically matching between the solutions close to the

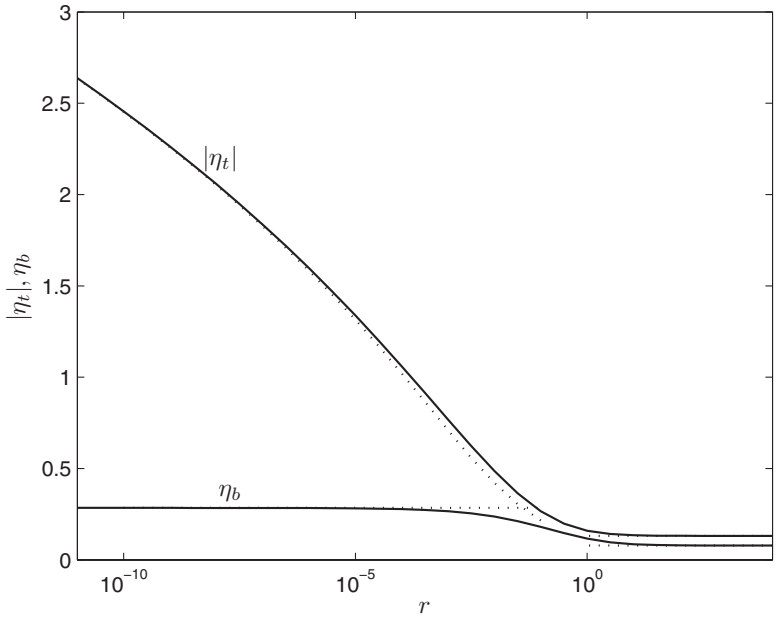

FIG. 17. The upper and lower contacts points of the interface with the underlying boundary, η_b and the free surface, η_t, as a function of the viscosity ratio between the fluids, r, for a wide channel (solid line). Also plotted are the asymptotic expressions for these positions in the regimes $r \gg 1$ and $r \ll 1$ (dotted lines).

boundary and within the interior. It turns out that the contribution from the region close to the lower boundary is asymptotically smaller and thus by imposing $\Phi_0(0) = 0$, we find that $\eta_t = -0.1312$ and $\eta_b = 0.0785$. The asymptotic forms in the regimes $r \ll 1$ and $r \gg 1$ are plotted in Figure 17 and shown to agree closely the exact numerical results.

[1] S. M. Taghavi, T. Seon, D. M. Martinez, and I. A. Frigaard, "Buoyancy-dominated displacement flows in near horizontal channels: the viscous limit," J. Fluid Mech. **639**, 1 (2009).
[2] T. Menand and J. C. Phillips, "Gas segregation in dykes and sills," J. Volcanol. Geotherm. Res. **158**, 393 (2007).
[3] H. A. Stone, A. D. Stroock, and A. Ajdari, "Engineering flows in small devices: microfluidics towards a lab-on-a-chip," Annu. Rev. Fluid Mech. **36**, 381 (2004).
[4] Y. Yamaguchi, T. Honda, M. P. Briones, K. Yamashita, M. Miyazki, H. Nakamura, and H. Maeda, "Influence of gravity on a laminar flow in a microbioanalysis system," Meas. Sci. Technol. **17**, 3162 (2006).
[5] P. G. Saffman and G. I. Taylor, "The penetration of fluid into a porous medium or Hele-Shaw cell containing a more viscous liquid," Proc. R. Soc. London, Ser. A **245**, 312 (1958).
[6] D. D. Joseph, R. Bai, K. P. Chen, and Y. Y. Renardy, "Core-annular flows," Annu. Rev. Fluid Mech. **29**, 65 (1997).
[7] T. S. Ng, C. J. Lawrence, and G. F. Hewitt, "Laminar stratified pipe flow," Int. J. Multiphase Flow **28**, 963 (2002).
[8] N. Brauner, J. Rovinsky, and D. M. Maron, "Analytical solution for laminar-laminar two-phase stratified flow in circular conduits," Chem. Eng. Commun. **141–142**, 103 (1996).
[9] B. A. Packham and R. Shail, "Stratified laminar flow of two immiscible fluids," Proc. Cambridge Philos. Soc. **69**, 443 (1971).
[10] H. S. Yu and E. M. Sparrow, "Stratified laminar flow in ducts of arbitrary shape," AIChE J. **13**, 10 (1967).
[11] J. Scoffoni, E. Lajeunesse, and G. M Homsy, "Interface instability during displacements of two miscible fluids in a vertical pipe," Phys. Fluids **13**, 553 (2001).
[12] C. S. Yih, "Instability due to viscosity stratification," J. Fluid Mech. **27**, 337 (1967).
[13] M. d'Olce, J. Martin, N. Rakotomalala, D. Salin, and L. Talon, "Convective/absolute instability in miscible core-annular flow. Part 1: Experiments," J. Fluid Mech. **618**, 305 (2009).
[14] F. Beckett, H. M. Mader, J. C. Phillips, A. Rust, and F. Witham, "An experimental study of low Reynolds number exchange flow of two Newtonian fluids in a vertical pipe," J. Fluid Mech. **682**, 652 (2011).
[15] H. E. Huppert and M. A. Hallworth, "Bi-directional flows in constrained systems," J. Fluid Mech. **578**, 95 (2007).
[16] R. R. Kerswell, "Exchange flow of two immiscible fluids and the principle of maximum flux," J. Fluid Mech. **682**, 132 (2011).
[17] T. Seon, J. Znaien, D. Salin, J. P. Hulin, E. J. Hinch, and B. Perrin, "Transient buoyancy-driven front dynamics in nearly horizontal tubes," Phys. Fluids **19**, 123603 (2007).
[18] J. Martin, N. Rakotomalala, L. Talon, and D. Salin, "Viscous lock-exchange in rectangular channels," J. Fluid Mech. **674**, 132 (2011).
[19] W. Didden and T. Maxworthy, "The viscous spreading of plane and axisymmetric gravity currents," J. Fluid Mech. **121**, 27 (1982).
[20] H. E. Huppert, "The propagation of two-dimensional and axisymmetric viscous gravity currents over a rigid horizontal surface," J. Fluid Mech. **121**, 43 (1982).
[21] J. Gratton and F. Minotti, "Self-similar viscous gravity currents: phase-plane formalism," J. Fluid Mech. **210**, 155 (1990).
[22] M. Dentz, D. M. Tartakovsky, E. Abarca, A. Guadadnini, Z. Sanchez-Vila, and J. Carrera, "Variable-density flow in porous media," J. Fluid Mech. **561**, 209 (2006).
[23] M. A. Hesse, H. A. Tchelepi, B. J. Cantwell, and F. M. Orr, "Gravity currents in horizontal porous layers: transition from early to late self-similarity," J. Fluid Mech. **577**, 363 (2007).
[24] J. M. Nordbotten and M. A. Celia, "Similarity solutions for fluid injection into confined aquifers," J. Fluid Mech. **561**, 307 (2006).
[25] H. E. Huppert and A. W. Woods, "Gravity-driven flows in porous layers," J. Fluid Mech. **292**, 53 (1995).
[26] R. E. Grundy and R. McLaughlin, "Eigenvalues of the Barenblatt-Pattle similarity solution in nonlinear diffusion," Proc. R. Soc. London, Ser. A **383**, 89 (1982).
[27] J. S. Mathunjwa and A. J. Hogg, "Self-similar gravity currents in porous media: linear stability of the Barenblatt-Pattle solution revisited," Eur. J. Mech. B/Fluids **25**, 360 (2006).
[28] G. K. Batchelor, *An Introduction to Fluid Dynamics* (Cambridge University Press, Cambridge, England, 1967), p. 615.
[29] D. Snyder and S. Tait, "A flow-front instability in viscous gravity currents," J. Fluid Mech. **369**, 1 (1998).
[30] A. J. Hogg and G. P. Matson, "Slumps of viscoplastic fluids on slopes," J. Non-Newtonian Fluid Mech. **158**, 101 (2009).